Electrochimica Acta 560 (2026) 148642

Contents lists available at ScienceDirect

Electrochimica Acta

journal homepage: www.journals.elsevier.com/electrochimica-acta

Green synthesis of $FeNi_3/FeNiO_x$ nanosponges via aluminum cementation for PGM-free anion exchange membrane water electrolysis

Francesko Malaj [a,b,*], Domenico Lentini [b,c], Alessandro Tampucci [b], Lorenzo Brogi [b], Raoul Cosenza [g], Enrico Berretti [d], Mohsin Muhyuddin [a], Emmanuel De Gregorio [h], Gianluigi Baiardi [e,f], Stiven Forti [e], Antonio Rossi [e], Camilla Coletti [e], Maddalena Corsini [g], Oreste Tarallo [c], Francesco Ruffo [c], Carlo Santoro [a,*]

[a] *Electrocatalysis and Bioelectrocatalysis Lab, Department of Materials Science, University of Milano-Bicocca, Via Roberto Cozzi 55, Building U5, 20125, Milan, Italy*
[b] *Ne.m.e.sys. s.r.l., via 2 Giugno 8, 50019 Sesto Fiorentino (Fi), Italy*
[c] *Department of Chemical Sciences, University of Naples Federico II, Complesso Univ. M.S. Angelo, Via Cintia, IT-80126, Naples, Italy*
[d] *Istituto di Chimica Dei Composti OrganoMetallici (ICCOM), Consiglio Nazionale Delle Ricerche (CNR), Via Madonna Del Piano 10, Sesto Fiorentino, 50019, Firenze, Italy*
[e] *Center for Nanotechnology Innovation @NEST, Istituto Italiano di Tecnologia, P.zza S. Silvestro 12, 56127, Pisa, Italy*
[f] *NEST Laboratory, Scuola Normale Superiore, P.zza S. Silvestro 12, 56127, Pisa, Italy*
[g] *Department of Biotechnology, Chemistry and Pharmacy, University of Siena, 53100, Siena, Italy*
[h] *Department of Engineering, University of Naples 'Parthenope', Centro Direzionale, Isola C4, 80143, Napoli, Italy*

ARTICLE INFO

Keywords:
Anion-exchange membrane water electrolysis
Non-noble metal electrocatalysts
Hydrogen evolution reaction
Oxygen evolution reaction

ABSTRACT

Low-temperature anion exchange membrane water electrolyzer (AEMWE) is widely recognized as a highly promising approach for sustainable hydrogen production. Nevertheless, current membrane–electrode assemblies (MEAs) still achieve their best performance when employing platinum group metal (PGM)-based electrocatalysts, while PGM-free alternatives generally exhibit inferior activity. In this study, a straightforward and unified synthetic route is presented for the preparation of non-noble metal electrocatalysts suitable for both the hydrogen and oxygen evolution reactions (HER and OER). The resulting electrocatalysts are composed of $FeNi_3/FeNiO_x$ nanosponges and were produced by a straightforward two-step synthetic route in aqueous solution, exploiting aluminum powder as a cementation agent. The developed electrocatalyst delivers overpotentials of 97 mV for the HER and 254 mV for the OER at a current density of 10 mA cm^{-2} in 1 M KOH, enabling a direct assessment of both mass-specific and geometric activities in comparison with PGM-based electrocatalysts. Beyond the initial electrochemical evaluation of the $FeNi_3/FeNiO_x$ material, the electrocatalyst was integrated into an MEA, operating as both the anode and the cathode and tested in an AEMWE. Under these conditions, the device achieved a cell voltage of 2.037 V at 1 A cm^{-2} and 50 °C, without iR correction. Notably, the resulting PGM-free MEA exhibited superior performance relative to a benchmark configuration employing Pt/C at the cathode and RuO_2 at the anode, with a voltage reduction of 105 mV at 1 A cm^{-2}. Long-term operation was evaluated over 150 h under a discontinuous power profile to gain insight into degradation behavior relevant to industrial operation. These results highlight a simple and scalable approach to the synthesis of earth-abundant electrocatalysts enabling high-performance AEMWE.

1. Introduction

Hydrogen is an essential industrial chemical, extensively utilized in processes such as ammonia production, petroleum upgrading, and metallurgical treatments [1]. More recently, it has gained increasing interest as a versatile energy vector and carbon-free fuel [1–3]. At present, most of the global hydrogen production is achieved from methane steam reforming, a process associated with substantial environmental issues. In 2022 alone, hydrogen production and consumption accounted for more than 900 million tonnes of CO_2 emissions [1]. As an alternative, water electrolysis has emerged as a sustainable route for hydrogen generation, particularly when integrated with electricity

* Corresponding authors.
E-mail addresses: f.malaj@campus.unimib.it (F. Malaj), carlo.santoro@unimib.it (C. Santoro).

https://doi.org/10.1016/j.electacta.2026.148642
Received 12 January 2026; Received in revised form 5 March 2026; Accepted 8 March 2026
Available online 11 March 2026

sourced from renewable energy systems [1]. Among the available electrolysis technologies, Proton Exchange Membrane Water Electrolyzers (PEMWEs) and Alkaline Water Electrolyzers (AWEs) are the most technologically mature and commercially deployed [4,5]. PEMWEs offer high operational flexibility, enabling elevate current densities with high energy efficiency. However, their reliance on highly acidic environments imposes the use of noble metal electrocatalysts, costly system components, and fluorinated polymer membranes, which collectively increase capital costs, raise environmental concerns, and limit large-scale deployment [6]. Conversely, AWEs represent a well-established and robust technology, benefiting from alkaline operating conditions that allow the use of more abundant and cost-effective materials with a lower environmental impact. Nonetheless, the conventional use of porous diaphragms for electrode separation leads to enhanced gas crossover, which poses significant challenges under dynamic and intermittent operating conditions typical of renewable energy integration [7,8]. In recent years, growing research interest has been directed toward anion exchange membrane water electrolyzers (AEMWEs). This technology integrates several key benefits derived from both PEMWE and AWE systems, including (i) suitability for operation under intermittent power input from renewable energy sources, (ii) the use of a non-porous and non-fluorinated polymer membranes that ensures effective physical separation of the electrodes while enabling internal hydrogen pressurization, (iii) the possibility of employing cost-effective, non-noble-metal electrocatalysts [2]. Despite these advantages, AEMWEs have not yet achieved widespread commercial deployment. Their limited large-scale implementation is primarily attributed to the insufficient long-term stability of membranes (AEMs) and ionomers (AEIs), as well as to the relatively low intrinsic activity of available electrocatalysts for both the anodic and cathodic reactions [9]. These limitations result in reduced overall efficiency when compared with state-of-the-art PEMWE [5]. During water electrolysis, the hydrogen evolution reaction (HER) occurs at the cathode, while the oxygen evolution reaction (OER) takes place at the anode. To reduce kinetic losses and enhance reaction rates, electrocatalysts are employed to decrease the associated overpotentials. Despite the alkaline operating environment, platinum group metals (PGMs) remain the benchmark electrocatalysts for both anodic and cathodic half-reactions. In particular, ruthenium dioxide (RuO_2) and platinum supported on carbon (Pt/C) are widely regarded as the state-of-the-art electrocatalysts for the OER and HER, respectively [10,11]. Despite their excellent electrocatalytic activity, these materials suffer from high costs and limited availability, being classified as critical raw materials (CRMs) by the European Union. These limitations significantly restrict their scalability and long-term sustainability. Consequently, the replacement of CRMs with more abundant and economically viable alternatives is a key requirement for the widespread implementation of this technology [12,13]. Among earth-abundant electrocatalysts, nickel-based materials have emerged as particularly promising candidates thanks to their low cost, adequate electrical conductivity, and excellent stability in alkaline environments. The activity of nickel-based electrocatalysts can be further improved through heteroatom or metal doping strategies. In this context, iron stands out as a particularly appealing dopant due to its high natural abundance and its well-documented ability to enhance electrocatalytic performance [14–16]. In our previous work, $FeNi_3/FeNiO_x$ nanoparticles prepared via chemical reduction using hydrazine demonstrated an overpotential of 234 mV for the OER at a current density of 10 mA cm^{-2} [17]. As highlighted in our previous study, several reports in the literature have investigated nickel–iron–based electrocatalysts for both the HER and OER, employing a variety of synthetic approaches [9]. Luo et al. reported the fabrication of a NiFe nanosheet film deposited onto nickel foam via electrodeposition, which functioned as a bifunctional electrocatalyst for both HER and OER. The resulting NiFe/NF electrode exhibited overpotentials of 139 mV at a current density of 10 mA cm^{-2} for the HER and 240 mV at 20 mA cm^{-2} for the OER [18]. Wei et al. synthesized $FeNi_3$ layered double hydroxide (LDH) nanosheets through the reduction of nickel and iron precursors in an autoclave at 120 °C for 12 h, followed by a CH_4 plasma treatment to anchor the material onto a carbon support and induce a phase transition from face-centred cubic (fcc) to hexagonal close-packed (hcp). The resulting hcp-phase electrocatalyst exhibited enhanced electrocatalytic performance, delivering overpotentials of 70 mV for the HER and 201 mV for the OER at a current density of 10 mA cm^{-2} [19]. A more straightforward route for the synthesis of these materials can be achieved through the low-temperature chemical reduction of nickel and iron salts in aqueous media using appropriate reducing agents. Such strategies offer the potential to decrease production costs and enable the large-scale fabrication of electrocatalysts for green hydrogen generation. Among these approaches, the reduction of metal ions on the surface of a less noble metal, commonly referred to as cementation, represents a particularly promising pathway. This method is already employed industrially for metal recovery and the purification of metal-ion-containing solutions [20–25]. In a previous study, we demonstrated the feasibility of this approach by synthesizing two types of nanostructured materials, namely $FeCo_3/FeCoO_x$ and $Ni_{1-x}Co_x/NiCoO_x$, which were evaluated as OER electrocatalysts and exhibited overpotentials of 288 mV and 296 mV, respectively, at a current density of 10 mA cm^{-2} [26]. Furthermore, the $Ni_{1-x}Co_x/NiCoO_x$ electrocatalyst was additionally evaluated in an ion-solvating membrane–based electrolyzer under different KOH concentrations [27]. Aluminum is especially attractive for cementation-based synthesis due to its strong reducing capability, low cost, and favorable environmental profile. Nevertheless, despite its significant potential, aluminum has remained largely unexplored for the preparation of electrocatalytic nanoparticles for water splitting [28].

In this study, we report, to the best of our knowledge, the first example of Ni_3Fe nanosponge synthesized via a feasible aqueous-phase route employing aluminum powder as the reducing agent and subsequently applied as a bifunctional electrocatalyst for both HER and OER. The obtained nanosponges were extensively characterized using high-resolution transmission electron microscopy (HRTEM), high-angle annular dark-field scanning transmission electron microscopy (HAADF-STEM), X-ray photoelectron spectroscopy (XPS), X-ray diffraction (XRD), X-ray fluorescence (XRF), and scanning electron microscopy (SEM). The $FeNi_3/FeNiO_x$ materials were then employed to fabricate electrodes capable of catalyzing both HER and OER in an AEMWE, exhibiting the overpotentials of 97 mV for the HER and 254 mV for OER, respectively, at a current density of 10 mA cm^{-2}. When integrated in a fully PGM-free MEA, the AEMWE delivered cell voltages of 2.037 V at 1 A cm^{-2} and 50 °C, without iR correction. Despite the higher electrocatalyst loading, these performances surpassed those obtained using a benchmark MEA based on PGM-based electrocatalysts, specifically Pt/C at the cathode and RuO_2 at the anode, with a voltage reduction of 105 mV at 1 A cm^{-2}. Furthermore, degradation behavior was investigated by subjecting the MEA to a discontinuous power profile representative of renewable energy operation. A durability test employing a daily power cycle over a total operation time of over 150 h. Overall, this work demonstrates the feasibility of employing a single nickel-based electrocatalyst for both HER and OER, offering significant advantages in terms of scalability and industrial flexibility, and enabling the development of high-performance, fully PGM-free MEAs for sustainable hydrogen production.

2. Materials and methods

2.1. Reagents

Iron(II) chloride tetrahydrate ($FeCl_2{\cdot}4\ H_2O$), nickel(II) chloride hexahydrate ($NiCl_2{\cdot}6\ H_2O$), ruthenium(IV) oxide (RuO_2, 99.9% metals basis), ethanol, polyvinyl alcohol (Mw 89,000-98,000 $gmol^{-1}$, 99% hydrolyzed), polytetrafluoroethylene 60 wt% dispersion in H_2O, sodium hydroxide (NaOH, 98%), and potassium hydroxide (KOH, purity 85%).

All chemicals were purchased from Sigma-Aldrich and used without additional purification. Aluminum powder (Al, 325 mesh, 99.5%) and platinum supported on carbon (Pt/C, 40 wt%) were purchased from Thermo Scientific and used without additional purification. Nafion™ dispersion D520CS was purchased from Ion Power and used without additional purification. As substrates and supports, carbon cloth porous transport layers (thickness 0.410 mm, Xiamen Zopin New Material Limited, China) and nickel foam (thickness 1.5 mm, Xiamen Tmax Battery Equipments Limited, China) were used. The AEM (AT-100) was kindly provided by Ne.m.e.sys. s.r.l. (Italy).

2.2. Synthesis $FeNi_3/FeNiO_x$ NPs

Step 1. $FeNi_3/FeNiO_x$ nanosponge was obtained via a wet chemical reduction route. $NiCl_2{\cdot}6\,H_2O$ (5.0 g, 21 mmol) and $FeCl_2{\cdot}4H_2O$ (1.0 g, 5.0 mmol) were dissolved in 50 mL of distilled water. After 5 minutes of stirring, the solutions were heated to 90 °C and aluminum powder (5 g) was introduced. An exothermic reaction with gas release occurred within a few minutes, and the mixtures were maintained at 90 °C until the water was completely evaporated. The resulting black powder was magnetically collected on one side of the vessel and thoroughly rinsed with water five times. In each cycle, the powder was first suspended, then magnetically decanted to eliminate non-magnetic residues.

Step 2. To separate the nanosponge from the surface of aluminum particles, the powders were redispersed in 100 mL of water at room temperature, followed by the addition of an excess of NaOH (50g) solution to dissolve the aluminum. After the gas evolution subsided, a washing sequence was carried out consisting of five rinses with distilled water and five additional washes with ethanol. In each cycle, the nanosponge was first suspended, then magnetically decanted to eliminate non-magnetic residues. After the final ethanol washing, the product was filtered and collected.

2.3. Preparation of electrode

2.3.1. Preparation of the standard electrodes for the LSV measurements

The anode was prepared by dispersing RuO_2 (0.024 g) in 200 μL of a 50:50 water/isopropanol mixture and mixing it with 44 μL of a 5% w/v alcohol Nafion dispersion, selected to ensure the formation of a homogeneous and stable catalyst ink (with an amount of Nafion 10wt% of the total solid content). The resulting ink was applied onto 6 cm^2 of nickel foam and dried overnight in an oven at 30 °C, yielding an electrode with an electrocatalyst loading of 4 mg cm^{-2}. The cathode was prepared by sonicating for 10 minutes a dispersion of 12.6 mg of Pt/C in 1000 μL of a solution composed of 28 μL of a 5% w/v alcohol Nafion dispersion, selected to ensure the formation of a homogeneous and stable catalyst ink (corresponding to 10 wt% Nafion with respect to the total solid content), and the remainder being a 50:50 water/isopropanol mixture. Then, 10 μL of the ink was applied onto 0.1 cm^2 of glassy carbon and dried at room temperature, yielding an electrode with a platinum loading of 0.5 mg cm^{-2}.

Pt/C and RuO_2 were employed as benchmark electrocatalysts for the HER and OER, respectively, owing to their well-established high electrocatalytic activity under alkaline conditions [10,11].

2.3.2. Preparation of the standard electrodes for the single-cell AEMWE tests

The anode was prepared by dispersing RuO_2 (0.020 g) in 200 μL of a 50:50 water/isopropanol mixture and mixing it with 37 μL of a 5% w/v alcohol Nafion dispersion, selected to ensure the formation of a homogeneous and stable catalyst ink (with an amount of Nafion 10wt% of the total solid content). The ink was applied onto 5 cm^2 of nickel foam and dried overnight in an oven at 30 °C, resulting in an electrode with an electrocatalyst loading of 4 mg cm^{-2}. The cathode was prepared by dispersing Pt/C ($6.3{\cdot}10^{-3}$ g) in 100 μL of a 50:50 water/isopropanol mixture and mixing it with 15 μL of a 5% w/v alcohol Nafion dispersion, selected to ensure the formation of a homogeneous and stable catalyst ink (with an amount of Nafion 10wt% of the total solid content), followed by sonication for 10 minutes. The ink was applied onto 5 cm^2 of carbon cloth and dried overnight at 50 °C, resulting in an electrode with a platinum loading of 0.5 mg cm^{-2}.

2.3.3. Preparation of the $FeNi_3/FeNiO_x$ electrode for the LSV measurements

The anode was prepared by dispersing $FeNi_3/FeNiO_x$ (0.150 g) in 800 μL of ethanol and mixing it with an aqueous PTFE dispersion (0.027 g, 60 wt%). The resulting ink was applied onto 6 cm^2 of nickel foam and dried overnight in an oven at 30 °C, yielding an electrode with a catalyst loading of 25 mg cm^{-2}. The cathode was prepared by sonicating for 10 minutes a dispersion of $FeNi_3/FeNiO_x$ (0.025 g) in 100 μL of a solution composed of 55 μL of a 5% w/v alcohol Nafion dispersion, selected to ensure the formation of a homogeneous and stable catalyst ink (corresponding to 10 wt% Nafion with respect to the total solid content), and the remainder being a 50:50 water/isopropanol mixture. Then, 10 μL of the ink was applied onto 0.1 cm^2 of glassy carbon and dried at room temperature, yielding an electrode with a $FeNi_3/FeNiO_x$ loading of 25 mg cm^{-2}.

2.3.4. Preparation of the $FeNi_3/FeNiO_x$ electrode for the single-cell AEMWE tests

The anode was prepared by dispersing $FeNi_3/FeNiO_x$ (0.125 g) in 500 μL of ethanol and mixing it with an aqueous PTFE dispersion (0.023 g, 60 wt%). The ink was applied onto 5 cm^2 of nickel foam and dried overnight in an oven at 30 °C, resulting in an electrode with a catalyst loading of 25 mg cm^{-2}. The cathode was prepared by sonicating for 5 minutes $FeNi_3/FeNiO_x$ (0.125 g) dispersed in 280 μL of an aqueous polyvinyl alcohol solution (10% w/v). The ink was applied onto 5 cm^2 of carbon cloth (PTL) and dried overnight at 30 °C, resulting in an electrode with a $FeNi_3/FeNiO_x$ loading of 25 mg cm^{-2}.

2.4. Electrochemical measurements

The electrochemical measurements for HER were carried out using a GAMRY Interface 1010B potentiostat/galvanostat (Gamry Instruments, Warminster, USA), while the OER measurements were carried out using an Arbin BT-G battery testing system (Arbin Instruments, USA). A Mini HydroFlex 80521 reversible hydrogen electrode (RHE, Gaskatel, Germany) was used as the reference electrode in a three-electrode configuration. Linear sweep voltammetry (LSV) measurements were recorded at a scan rate of 5 mV s^{-1} under constant stirring at 600 rpm to prevent gas bubble accumulation on the electrodes, at room temperature. Before acquiring the LSV data, the electrodes were activated through cyclic voltammetry (CV), applying a potential window between 1.2 V and 1.8 V versus RHE for OER and between 0.02 V and −0.5 V versus RHE for HER, at a scan rate of 50 mV s^{-1}, until a stable CV curve was obtained. The overpotentials of the electrocatalyst were determined from the LSV curves and were estimated at a current density of 10 mA cm^{-2}. Tafel plots were derived from the LSV data by plotting the applied potential as a function of the logarithm of the current density. All measured potentials were corrected for the ohmic drop (iR compensation) before constructing Tafel plots. The Tafel slope was obtained by linear fitting in the kinetically controlled region.

Overall, water electrolysis tests were conducted in a single-cell AEMWE with an active area of 5 cm^2 (H5, Antares Electrolysis S.r.l., Italy), equipped with nickel end plates, a bipolar plate, and a plastic frame. The performance of the $FeNi_3/FeNiO_x$ electrocatalyst synthesized in this study was compared with that of platinum on carbon (Pt/C) for HER and RuO_2 for OER, by acquiring polarization curves at 50 °C. The MEA was made by inserting the AT-100 membrane between the anode and cathode and compressing it with a pressure of 2 MPa. Before the assembly, the membrane was activated in a 1 M KOH solution for 24

hours, thus reaching a thickness of 60 μm. The electrodes, instead, were immersed in a 1 M KOH solution for 30 minutes. The electrolyte used was an aqueous 1 M KOH solution, circulated through a peristaltic pump at a flow rate of 48 mL min^{-1}. The polarization curves were recorded by applying current steps and simultaneously measuring the cell voltage using a Hioki 3560 AC mW HiTester (Hioki Corporation, Japan). Finally, an analysis of the degradation trend of the $FeNi_3/FeNiO_x$ MEA under intermittent power supply was carried out. The AEMWE was subjected to a daily operating protocol consisting of continuous operation at a current density of 0.4 A cm^{-2} for approximately 8–9 h. Each operating cycle included controlled ramp-up and ramp-down steps at 0.2 A cm^{-2}, each lasting 30 min, which were not counted within the total 153 h of operation. After completion of each daily cycle, the system was left at open circuit overnight with no applied current.

2.5. Characterization methods

2.5.1. XPS analysis

XPS measurements were performed using a Specs XR50 source with an Al anode at a power of 300 W. The analyzer employed was a Specs Astraios 190 with a 2D-CMOS detector and a 3×25 mm entrance slit. All scans were acquired in normal emission conditions and at room temperature. The survey scans were performed at a pass energy of 50 eV, whereas all high-res scans were performed at a pass energy of 10 eV. The binding energies of the spectra have been referenced to the position of the adventitious carbon C 1s at 285.2 eV. All spectra were first elaborated by complementing Shirley or Tougaard backgrounds with a linear component due to inelastically scattered electrons from XPS signals at lower binding energies. Subsequently, envelopes associated with metals, oxides, and hydroxides were reproduced with few mutually constrained symmetric Gaussian-Lorentzian sums (for non-metallic compounds) or asymmetric Lorentzian profiles (for metallic states) and fitted to the data. The employed components have been grouped in main line and the satellite envelope for clarity of visualization. Standard spin doublet constraints were enforced.

2.5.2. XRD analysis

Crystallographic analysis was carried out using XRD with a Rigaku Miniflex 600 instrument equipped with a copper source, operating over a 2θ range from 10° to 90°.

2.5.3. XRF analysis

Qualitative inorganic elemental analysis was performed using XRF with an Artax 200 instrument (Bruker, Billerica, MA, USA) equipped with a molybdenum anode.

2.5.4. SEM analysis

Morphological characterization of the electrocatalyst was conducted using a desktop SEM (Thermo Fisher Phenom G6, Eindhoven, The Netherlands) equipped with a thermionic CeB_6 source, capable of operating within a magnification range of 400x to 70,000x.

2.5.5. HRTEM analysis

HRTEM images were obtained using a Thermo Fisher Talos F200X G2 operated at an accelerating voltage of 200 kV, equipped with a high-speed CETA camera at a resolution of 4096 × 4096 pixels and without an objective aperture. HAADF images were captured using a Panther annular STEM detector with a convergent beam angle of 10.5 mrad and a camera length of 330 mm. EDX mapping was performed with a Super X spectrometer fitted with four 30 mm^2 silicon drift detectors, providing a collection angle of 0.7 srad.

3. Results and discussion

3.1. Synthesis and characterization

As already discussed in our previous work, cementation can be described as a coupled chemical–physical process in which metal ions dissolved in solution are reduced and deposited onto the surface of a less noble metal [28]. Although metallic aluminum possesses a highly negative standard redox potential (Al^{3+}/Al, −1.66 V), markedly lower than those of Fe^{2+}/Fe (−0.44 V) and Ni^{2+}/Ni (−0.25 V), its effectiveness as a reducing agent in aqueous media is strongly limited by the rapid formation of a thin, electrically insulating oxide layer on its surface. This passivation process occurs within a nanosecond timescale and significantly suppresses aluminum reactivity, particularly under near-neutral pH conditions [29]. To overcome this limitation, chloride-based metal precursors were employed. Chloride anions are known to promote pitting corrosion on aluminum surfaces even in neutral aqueous environments. At approximately neutral pH, the native aluminum oxide layer is believed to carry a net positive charge, which favors the electrostatic adsorption of chloride ions. These anions penetrate the oxide film and reach the underlying metallic aluminum, where localized oxidation and dissolution occur in the presence of confined water molecules. As a consequence, a mildly acidic microenvironment is generated at the metal–solution interface, which prevents oxide layer reformation and sustains continuous aluminum oxidation, electron release, and simultaneous hydrogen evolution. The hydrogen radicals produced during this process act as reactive intermediates, diffusing toward the solution interface and reducing the dissolved metal ions, thereby initiating nanosponge nucleation and growth, as previously reported [28, 29].

The evolution of the reaction can be effectively monitored by acquiring SEM images at different stages of the process. During step 1, pristine aluminum particles (Fig. 1a) become progressively coated with a Ni_3Fe nanosponge layer formed via cementation (Fig. 1b). In step 2, alkaline treatment with NaOH promotes the solubilization of the residual aluminum through the formation of aluminate species, as described by Eq. 1, ultimately leaving behind a hollow $FeNi_3/FeNiO_x$ shell structure (Fig. 1c).

$$2\,Al_{(s)} + 6\,H_2O_{(l)} + 2\,OH^-_{(aq)} \rightarrow 2\,[Al(OH)_4]^-_{(aq)} + 3\,H_{2(g)} \quad (1)$$

In both reaction steps, the process is exothermic and accompanied by gas evolution, occurring simultaneously with the formation of a fine black powder. From a practical viewpoint, the methodology is straightforward, without the use of a capping agent, requires minimal equipment, and reactions are completed within a few minutes, followed by rapid work-up. According to the work of Lu et al. [30], when the Ni/Fe molar ratio is below 3, nanoparticles exhibit both the $FeNi_3$ alloy and crystalline Fe_4O_3, whereas a ratio of exactly 3 results exclusively in $FeNi_3$ formation. In our study, to promote the appearance of an amorphous phase within the nanoparticles, we adopted a Ni/Fe ratio of 4. This excess of nickel, as previously demonstrated in our earlier work, beyond the stoichiometric requirement for alloy formation, enabled the coexistence of amorphous nickel and iron oxides. Such a configuration is beneficial, as it enhances the electrocatalytic performance for HER and OER [31–34].

XRF analysis confirmed the simultaneous presence of nickel and iron, thereby verifying the incorporation of both metals into the electrocatalyst (Fig. S1).

The XRD profile reported in Fig. 2 is dominated by three intense reflections appearing at approximately 44.5°, 51.7°, and 76.3° (2θ). These diffraction features are consistent with those reported for $FeNi_3$ (JCPDS Card No. 38-0419, awaruite). Indexing of the peaks allows their assignment to the (111), (200), and (220) crystallographic planes, corresponding to d-spacings of 2.05 Å, 1.77 Å, and 1.25 Å, respectively. The observed diffraction pattern is therefore characteristic of a face-centered

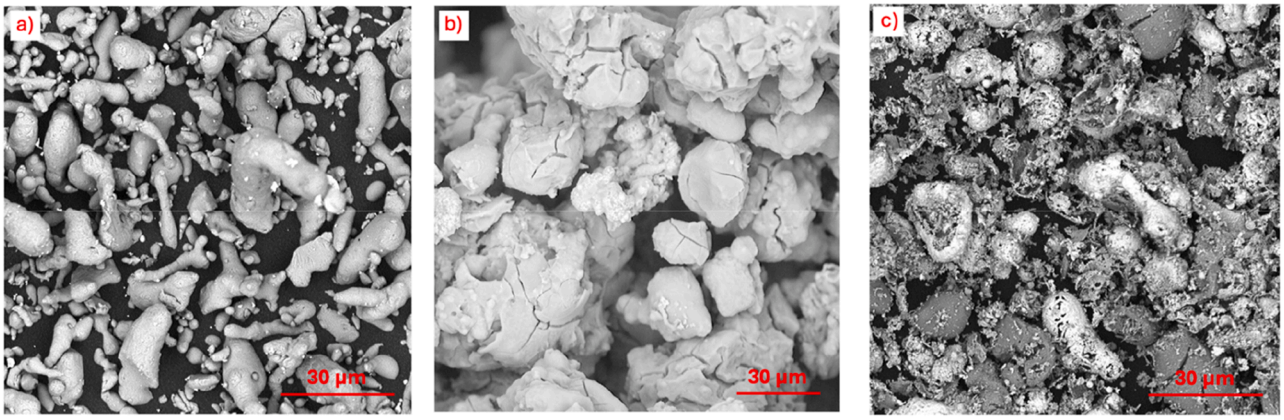

Fig. 1. SEM images at different magnifications of: (a) raw aluminum powder. (b) $FeNi_3/FeNiO_x$ formed on aluminum powder after cementation; (c) $FeNi_3/FeNiO_x$ aggregates after aluminum removal.

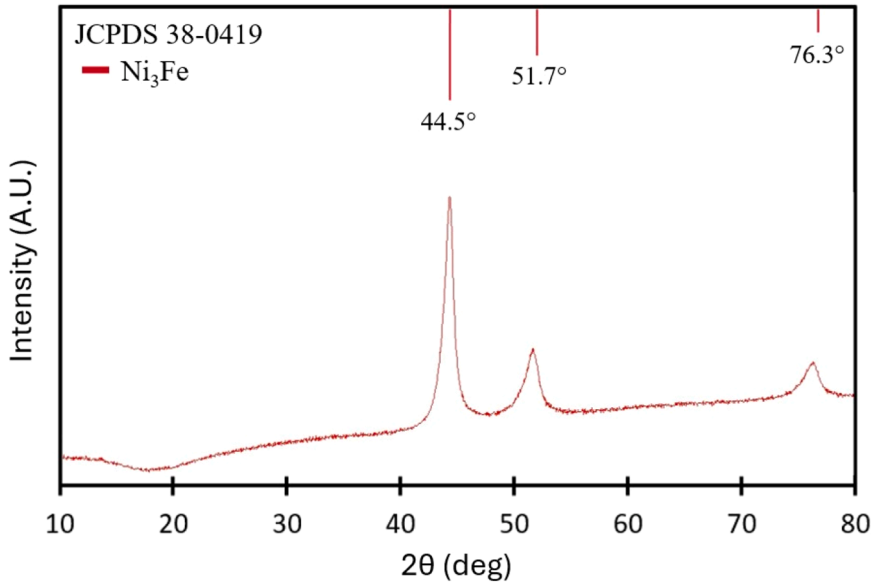

Fig. 2. XRD pattern of the synthesized nanosponge.

cubic (fcc) $FeNi_3$ alloy, in which nickel atoms preferentially occupy the face-centered lattice sites, while iron atoms are located at the cube corners [35]. In addition to the crystalline reflections, the diffractogram displays peak broadening accompanied by a modulated background

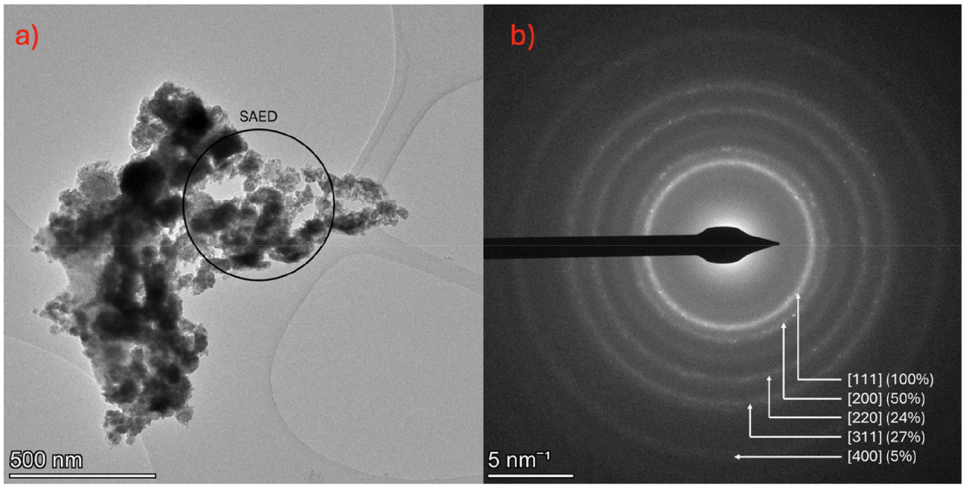

Fig. 3. (a) HR-TEM analysis of $FeNi_3/FeNiO_x$ (b) SAED showing main reflexes for thr $FeNi_3$ phase.

signal, which suggests the presence of poorly ordered or amorphous phases. Nevertheless, as XRD does not allow a definitive identification of amorphous components, this observation should be interpreted cautiously and corroborated by complementary characterization techniques.

HRTEM (Fig. 3a) showed sponge-like agglomerates with non-homogeneity in size and morphology. The selected area electron diffraction (SAED) pattern acquired from the circled region (Fig. 3b) shows well-defined diffractionrings, corresponding to the (111), (200), (220), (311), and (400) reflections of a face-centered cubic of Ni_3Fe, confirming the high level of crystallinity seen by XRD. STEM EDS mapping (Fig. 4) confirmed the presence of nickel and iron along with oxygen. In addition, EDS highlighted a trace of aluminum incorporated into the nanoparticle matrix, most likely as amorphous oxide, with an estimated atomic fraction below 1%.

STEM EDS analysis of $FeNi_3/FeNiO_x$ nanosponge (Fig. 5 and Table 1) enabled the estimation of an average Ni:Fe:O molar ratio of approximately 5:1:4. These stoichiometric values were subsequently used to calculate the reaction yields by comparing the mass of precursor salts with that of the final washed and dried powders (after the second step) for three independent synthesis batches. The results, summarized in Table S1, indicate reaction yields of 86.8% for $FeNi_3/FeNiO_x$. The observed mass loss may arise from a combination of incomplete cementation and minor material losses during washing and handling steps. A minor residual Al content (1.09 %) was detected by EDS. Although partial dissolution under alkaline conditions cannot be excluded, the electrolyte was renewed at each restart during the durability test, minimizing possible accumulation effects.

Fig. 6 reports the XPS high-resolution scans in the 2p-core-level energy ranges of nickel (Fig. 6a) and iron (Fig. 6b) and in two distinct core-level energy ranges of aluminum (Fig. 6c and d), partially overlapped with nickel. The overall high binding energies of the detected signals suggest a predominantly oxidized surface of the particles, consistent with the O 1s signal visible in the survey scan in Fig. S2. The shape and width of the main peaks further imply a non-trivial chemical composition and the necessity to consider the overlap of multiple envelopes related to oxides, oxyhydroxides, and hydroxides of the metals under investigation, each of them shifted with respect to the previous one according to variations in the screening of the nuclear charge. Ordinary envelopes for each compound were thus reproduced from references [36–40], by including components related to main transitions and shake-up satellites in the covalently bound compounds, which are separately plotted. In Fig. 6a, the signal detected from the Ni 2p level can be fully explained in terms of Ni oxides (~10%), NiOOH (~35%), and Ni $(OH)_2$ (~55%) envelopes. Conversely, the spectrum of Fe 2p in Fig. 6b is compatible with a fraction of the atoms persisting in the metallic state (<15%), while the rest can be attributed to iron oxides (~15%) and

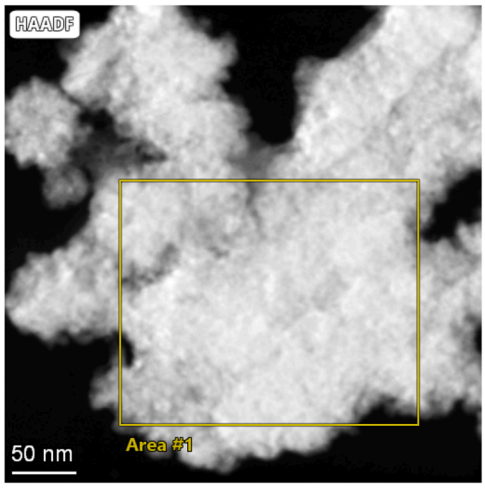

Fig. 5. Area of the sample used to extract atomic percentages of the sample via EDS.

Table 1
Corresponding elemental atomic ratios of the STEM EDS area in the $FeNi_3/FeNiO_x$ sample.

Atomic fraction [%]				
C	O	Al	Fe	Ni
30.85	27.26	1.09	6.39	34.39

(oxy)hydroxides (~70%). The scans in Fig. 6c and d were aimed at ascertaining the presence of aluminum residues on the particles' surface. However, adopting the Ni 3s and Ni 3p envelopes of the Ni compounds identified in the Ni 2p range leads to the conclusion that aluminum is absent from the sample, at least within the limits of the lower signal-to-noise ratio, which is consistent with EDX measurements. The identified backgrounds include a linear component to model the contribution from inelastically scattered electrons at lower binding energies. Standard spin doublet constraints were enforced, and the resulting components are aggregated within the individually plotted lineshapes.

In Figures S3, SEM micrograph of the prepared electrodes are reported, confirming the complete coating of the porous transport layer (PTL). This means that the catalyst and binder work well together, which leads to even mixing and strong adhesion to the support. At a higher magnification, the surface of the electrode showed cracks, rough textures and local inhomogeneities. These structural irregularities are

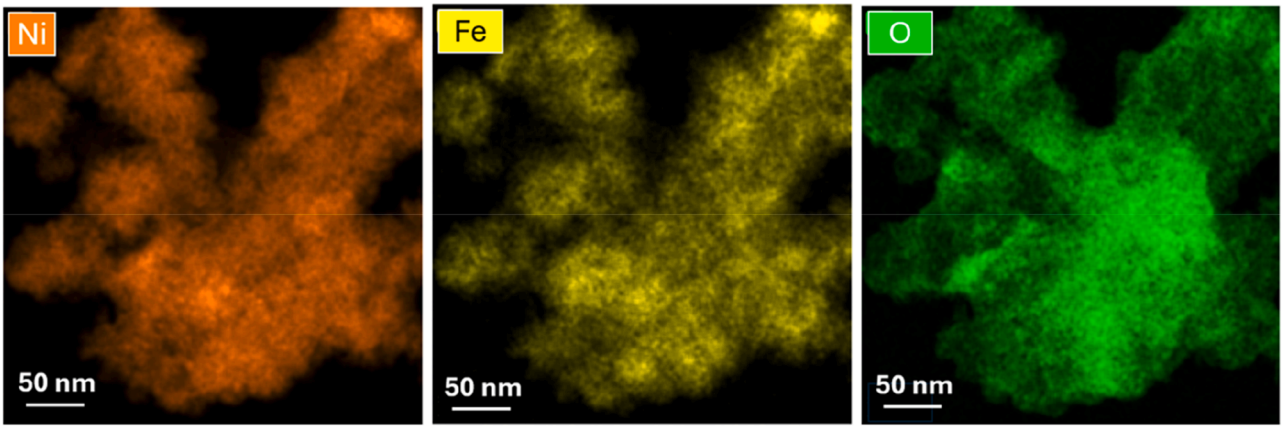

Fig. 4. Elemental mapping of $FeNi_3/FeNiO_x$ obtained by EDX.

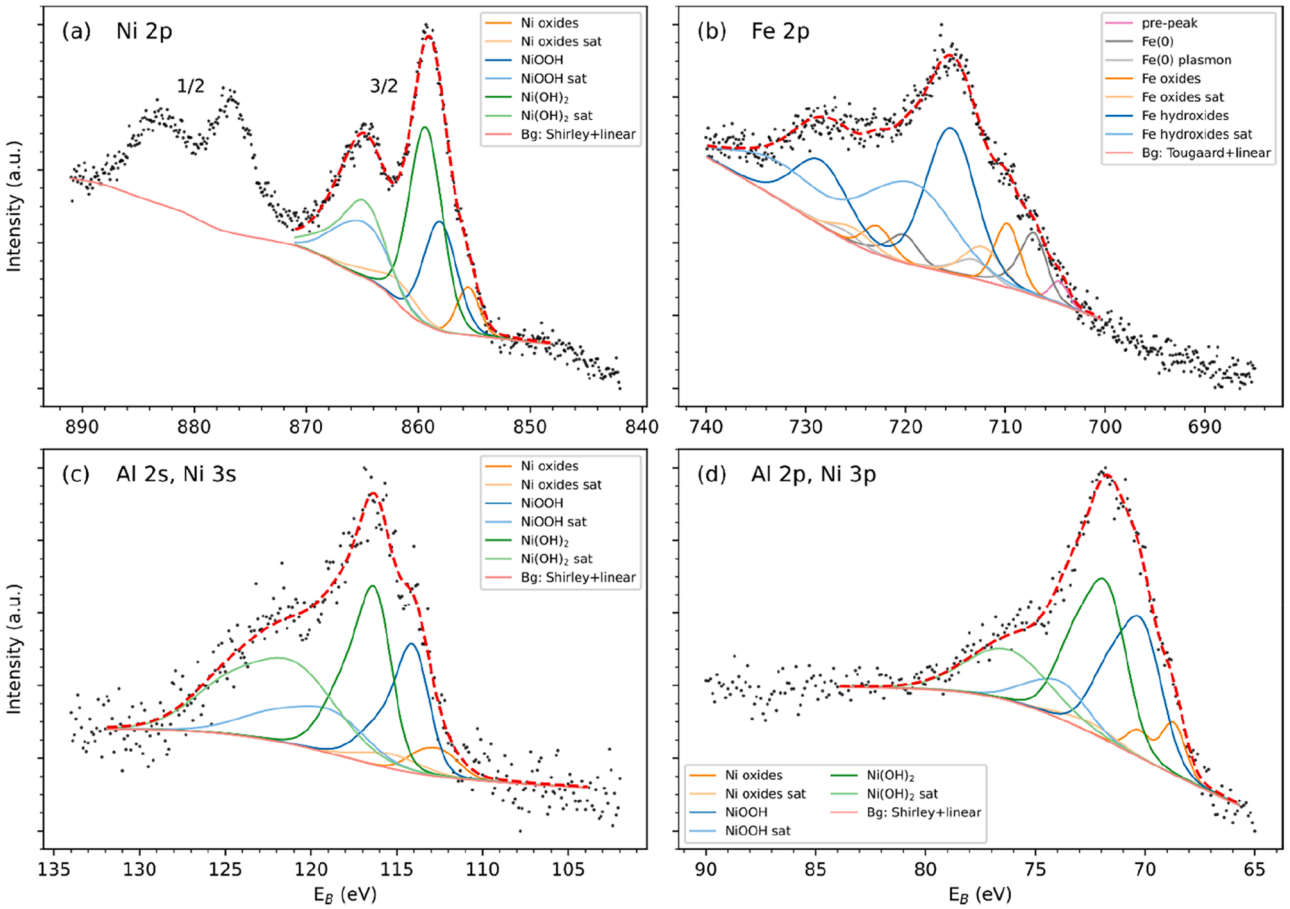

Fig. 6. XPS high-resolution scans of (a) Ni 2p, (b) Fe 2p, (c) Al 2s - Ni 3s, and (d) Al 2p - Ni 3p. The backgrounds include a linear component due to inelastically scattered electrons at lower binding energies. "sat" refers to the shake-up satellites.

advantageous, as they increase the available surface area, improve mass transport, and facilitate the release of gaseous products, thereby boosting both OER and HER activity [41].

3.2. Electrochemical activity

The electrocatalytic behavior of $FeNi_3/FeNiO_x$ toward HER and OER was initially examined through LSV in 1 M KOH using a conventional three-electrode configuration, while kinetic parameters were assessed via Tafel slope analysis. For comparison, commercial RuO_2 and Pt/C were employed as benchmark electrocatalysts for OER and HER, respectively, and tested under identical experimental conditions. In all cases, the electrocatalyst loading on the electrode surface was kept constant, as specified in the "Materials and Methods" section. To further investigate the potential of $FeNi_3/FeNiO_x$ in low-temperature water electrolysis, single-cell AEMWE experiments were performed. Polarization curves were recorded at 50 °C using 1 M KOH as the electrolyte.

Due to the higher availability of precursors, low production costs,

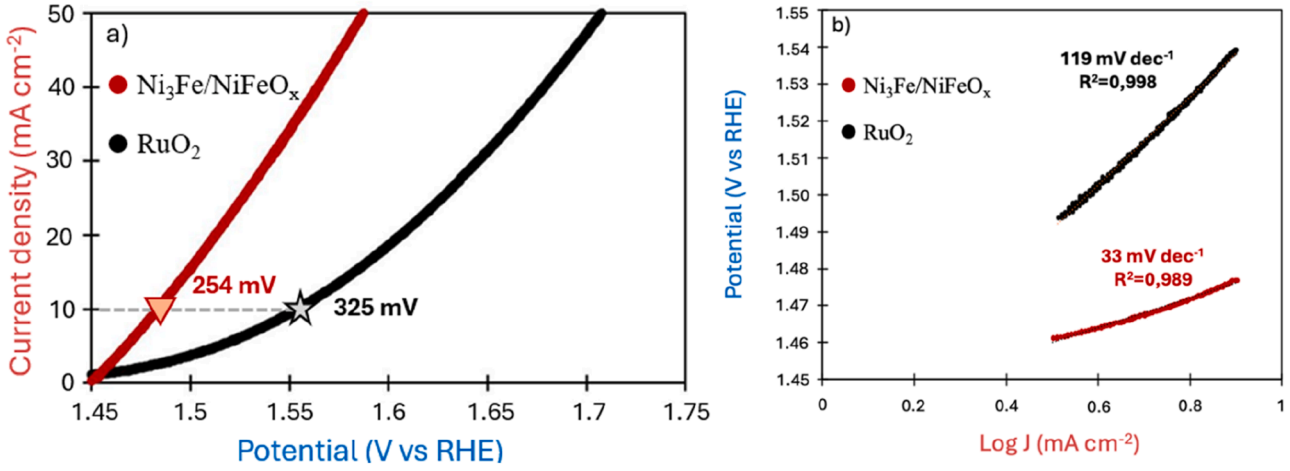

Fig. 7. (a) LSV curves of $FeNi_3/FeNiO_x$ (red) and RuO_2 (black) as OER electrocatalysts in 1.0 M KOH at 5 mV s^{-1} scan rate. (b) Tafel slope analysis for OER electrocatalysts: $FeNi_3/FeNiO_x$ (red) and RuO_2 (black).

and the simple synthetic route of $FeNi_3/FeNiO_x$ nanosponge, a larger electrocatalyst loading was employed relative to that of PGM-based references, simulating a scenario more aligned with industrial practice. Nevertheless, both mass activity and geometric activity [42] were evaluated to provide a normalized comparison, as reported in Fig. 11.

3.3. Oxygen evolution reaction of $FeNi_3/FeNiO_x$ electrocatalysts

Fig. 7 compares the OER electrocatalytic behavior of $FeNi_3/FeNiO_x$ nanosponge and commercial RuO_2 through their polarization responses. Under identical testing conditions, the $FeNi_3/FeNiO_x$ catalyst reaches the reference current density of 10 mA cm^{-2} at a substantially lower anodic overpotential than RuO_2. Specifically, $FeNi_3/FeNiO_x$ requires 254 mV, whereas RuO_2 exhibits a significantly higher value of 325 mV, resulting in a performance advantage of 71 mV for the Ni–Fe–based material (Fig. 7a).

Further insight into the reaction kinetics was obtained from Tafel analysis. The $FeNi_3/FeNiO_x$ catalyst shows a markedly smaller Tafel slope of 33 mV dec^{-1} compared to 119 mV dec^{-1} for RuO_2 (Fig. 7b), indicating faster charge-transfer kinetics and more efficient OER catalysis.

Both electrocatalysts were further evaluated at the device level by incorporating them as anode electrocatalysts in MEAs, while Pt/C was employed at the cathode. The resulting MEAs were tested in a single-cell AEMWE operated at 50 °C, and their polarization behavior is reported in Fig. 8 and Table 2. Across the entire investigated current density range, the cell assembled with $FeNi_3/FeNiO_x$ consistently operated at lower voltages than the corresponding RuO_2-based system. The voltage advantage of the $FeNi_3/FeNiO_x$ anode averaged approximately 203 mV and became more pronounced at higher current densities, increasing from 203 mV at 0.4 A cm^{-2} to 266 mV at 1 A cm^{-2}. This trend indicates more favorable anodic kinetics for $FeNi_3/FeNiO_x$ under high-rate operating conditions.

The superior performance observed at the cell level confirms the high OER activity of $FeNi_3/FeNiO_x$, in agreement with previous reports on Ni–Fe oxide–based alloy electrocatalysts [43–45]. It should be noted that the electrocatalyst loading employed for $FeNi_3/FeNiO_x$ was higher than that used for RuO_2. While this partially offsets the intrinsically higher mass activity of the noble-metal benchmark, it results in an enhanced geometric activity, as illustrated in Fig. 11. This strategy is commonly adopted for PGM-free OER electrocatalysts operating in alkaline environments [42] and, in the present case, represents a practical and justified trade-off considering the low cost and straightforward

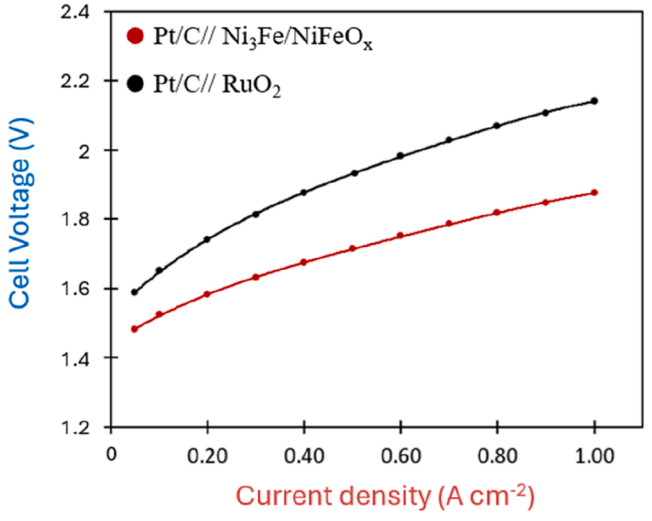

Fig. 8. Polarization curve of AEMWE single cells with Pt/C || RuO_2 and Pt/C || $FeNi_3/FeNiO_x$, tested at 50 °C without iR correction.

Table 2
Electrocatalytic performance of noble and non-noble MEA in AEM cells at 50 °C.

Anode	Cathode	V at 0.4 A cm^{-2}	V at 0.6 A cm^{-2}	V at 1 A cm^{-2}
$FeNi_3/FeNiO_x$	Pt/C	1.674	1.751	1.876
RuO_2	$FeNi_3/FeNiO_x$	2.029	2.115	2.334
RuO_2	Pt/C	1.877	1.982	2.142
$FeNi_3/FeNiO_x$	$FeNi_3/FeNiO_x$	1.829	1.899	2.037

synthesis of $FeNi_3/FeNiO_x$.

3.4. Hydrogen evolution reaction of $FeNi_3/FeNiO_x$ electrocatalysts

Fig. 9 illustrates the HER polarization behavior of $FeNi_3/FeNiO_x$ in comparison with the Pt/C benchmark. In contrast to the trend observed for the OER, the nickel–iron–based electrocatalyst does not achieve superior HER performance, even when employed at higher electrocatalyst loadings. As highlighted in Fig. 11, $FeNi_3/FeNiO_x$ remains inferior to Pt/C in terms of both mass-specific and geometric activity. At a current density of 10 mA cm^{-2}, $FeNi_3/FeNiO_x$ requires an overpotential of 97 mV, whereas Pt/C reaches the same current at only 27 mV, resulting in a performance gap of approximately 70 mV (Fig. 9a). Kinetic analysis further emphasizes this difference. The Tafel slope derived for Pt/C is 66 mV dec^{-1}, significantly lower than the 126 mV dec^{-1} measured for $FeNi_3/FeNiO_x$ (Fig. 9b), indicating faster reaction kinetics on the noble-metal electrocatalyst. This disparity suggests distinct rate-determining steps for the two materials, with $FeNi_3/FeNiO_x$ exhibiting slower hydrogen evolution (HER) at the electrode interface, likely associated with less efficient water dissociation and hydrogen adsorption processes within the Volmer–Heyrovsky mechanism.

Single-cell AEMWE tests were further conducted by employing RuO_2 as the anode electrocatalyst, while $FeNi_3/FeNiO_x$ and Pt/C were alternatively used at the cathode. The resulting polarization behavior, recorded at an operating temperature of 50 °C, is reported in Fig. 10 and Table 2. In agreement with the trends observed in half-cell measurements, the AEMWE assembled with $FeNi_3/FeNiO_x$ at the cathode exhibited systematically higher cell voltages compared to the Pt/C-based configuration. The voltage difference between the two systems averaged approximately 148 mV over the investigated current density range and became more pronounced at higher currents, increasing from 152 mV at 0.4 A cm^{-2} to 192 mV at 1 A cm^{-2}. This outcome highlights that, despite significant progress in PGM-free electrocatalyst development, Pt/C still represents the most effective cathodic material for the HER. The persistent performance gap can be rationalized by considering the fundamental requirements of HER electrocatalysis, which are strongly governed by the adsorption strength of hydrogen intermediates on the electrocatalyst surface. According to the Sabatier principle, optimal HER activity is achieved when hydrogen adsorption is neither too strong nor too weak, allowing a balanced interplay between

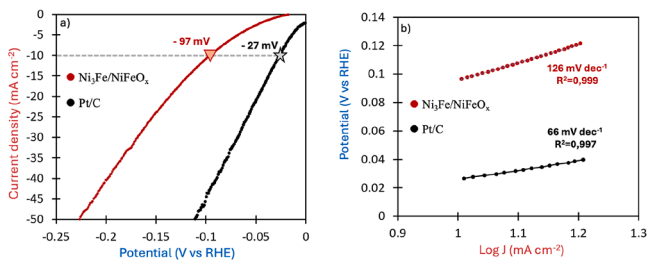

Fig. 9. (a) LSV curves of $FeNi_3/FeNiO_x$ (red) and Pt/C (black) as HER electrocatalysts in 1.0 M KOH at 5 mV s^{-1} scan rate. (b) Tafel slope analysis for HER electrocatalysts: $FeNi_3/FeNiO_x$ (red) and Pt/C (black).

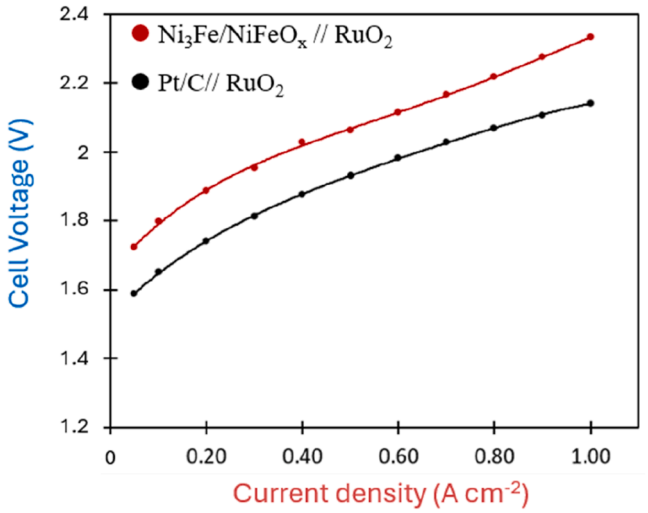

Fig. 10. Polarization curve of AEMWE single cells with Pt/C || RuO_2 and $FeNi_3/FeNiO_x$ || RuO_2, tested at 50 °C without iR correction.

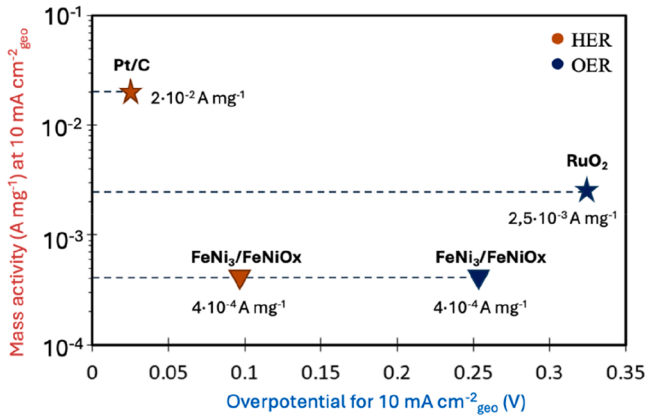

Fig. 11. Evaluation of mass activity and overpotential at 10 mA cm^{-2} for HER and OER electrocatalysts.

activation and desorption steps. This criterion is commonly quantified by the Gibbs free energy of hydrogen adsorption, ΔG(H*), with values close to the thermoneutral condition (ΔG(H*) ≈ 0 eV) being ideal. Density functional theory calculations reported by Ni et al. indicate a ΔG (H*) value of 0.48 eV for Ni_3Fe, whereas platinum exhibits a value close to zero, accounting for its exceptional HER activity and its role as the benchmark electrocatalyst over a wide pH range [46–48]. No pre-reduction treatment was applied prior to HER measurements, as the catalyst was designed to operate as a bifunctional material without additional activation steps, in view of process simplification and potential scalability. While partial electrochemical reduction of surface oxides under cathodic polarization cannot be excluded, detailed investigation of surface evolution during HER was beyond the scope of this work.

3.5. AEMWE test with electrocatalysts fully PGM-free

The device-level performance of an AEMWE assembled using $FeNi_3/FeNiO_x$ nanosponge as a single, bifunctional electrocatalyst at both electrodes was systematically investigated and benchmarked against a conventional MEA comprising Pt/C at the cathode and RuO_2 at the anode (Fig. 12 and Table 2). Polarization curves were recorded in 1 M KOH at an operating temperature of 50 °C. At low current densities, up to approximately 0.2 A cm^{-2}, the voltage response of the fully PGM-free

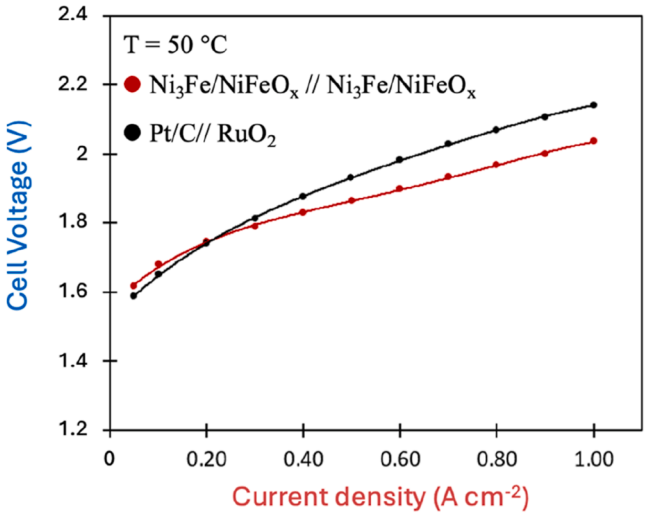

Fig. 12. Polarization curves of AEMWE single cells with Pt/C || RuO_2 and $FeNi_3/FeNiO_x$ || $FeNi_3/FeNiO_x$, tested at 50 °C without iR correction.

MEA closely overlapped with that of the noble-metal-based reference. Beyond this regime, the $FeNi_3/FeNiO_x$-based system exhibited progressively lower operating voltages. This trend indicates that, at elevated current densities, the enhanced OER activity of $FeNi_3/FeNiO_x$ effectively compensates for its comparatively slower HER kinetics. This effect is particularly relevant given that the OER, involving a four-electron transfer, largely governs the overall cell overpotential [49]. With increasing current density, the voltage advantage of the PGM-free configuration became more pronounced, increasing from 48 mV at 0.4 A cm^{-2} to 105 mV at 1 A cm^{-2} at 50 °C. Notably, the AEMWE equipped with the bifunctional $FeNi_3/FeNiO_x$ electrocatalyst achieved a cell voltage of 2.037 V at 1 A cm^{-2}, underscoring the strong potential of this fully PGM-free MEA for high-current-density operation.

A summary of the results from the polarization curves recorded at 50 °C in 1 M KOH electrolyte is presented in Table 2.

3.6. Degradation trend

Fig. 13 shows the degradation trend of the MEA employing $FeNi_3/FeNiO_x$ at both the anode and cathode, which was assessed by examining its response to intermittent power operation. This testing protocol was specifically designed to mimic the intermittent operation associated with renewable energy sources, while simultaneously imposing repeated start-up and shut-down stresses on the electrode assemblies.

The extent of performance degradation after 153 h of operation was evaluated by comparing the polarization curves collected at the beginning and at the end of the durability test (Fig. 14). The cell voltage increased by 195 mV at a current density of 0.4 A cm^{-2} and by 395 mV at 1 A cm^{-2}, respectively.

Although this experiment was carried out at the small scale and offers valuable insight into degradation tendencies, it should not be regarded as a comprehensive durability assessment from an industrial perspective, where a broader range of operating conditions and significantly longer testing durations are required. The observed voltage increase indicates that further optimization of the catalyst layer and MEA architecture is required to improve long-term stability. The present study focuses on validating the synthetic strategy rather than delivering an optimized industrial device.

4. Perspective and outlook

Hydrogen generated by water electrolysis using renewable electricity has the potential to challenge conventional, carbon-intensive

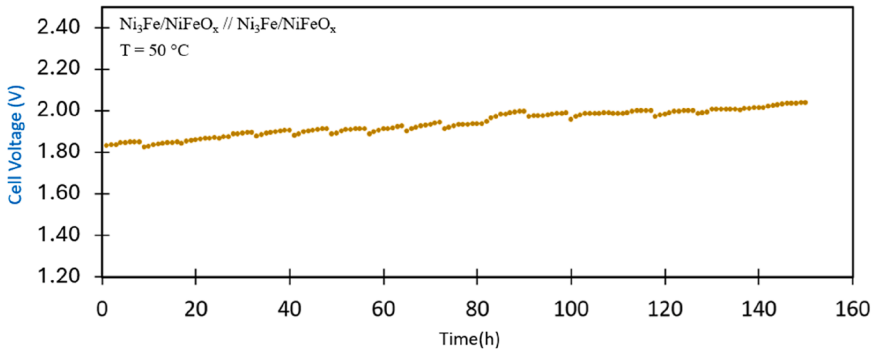

Fig. 13. Stability trend of $FeNi_3/FeNiO_x$ MEA under intermittent power supply.

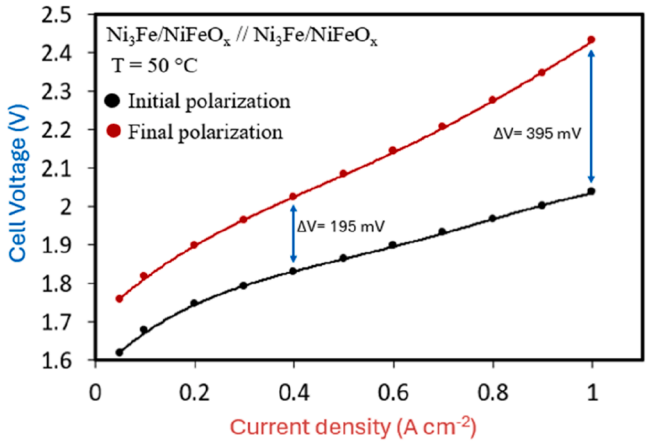

Fig. 14. Comparison of polarization curves for AEMWE employing $FeNi_3/FeNiO_x$ || $FeNi_3/FeNiO_x$, before and after 153 h of testing.

production routes. Achieving this goal and enabling hydrogen to assume a key role as a low-carbon energy vector in the energy transition requires the large-scale deployment of low-temperature electrolysis technologies. Such progress will critically depend on substantial cost reductions, simplified manufacturing pathways, and a reduced environmental impact throughout the production chain [50,51]. Addressing these challenges requires the development of electrocatalysts obtainable through simple, scalable, and environmentally benign synthetic routes, capable of delivering high electrocatalytic performance without the use of noble metals. In this context, the present work introduces a green and still scarcely explored synthetic strategy for the preparation of electrocatalysts for AEMWE. The approach described in the article was employed to synthesize a nanosponge material based exclusively on earth-abundant, non-noble metals, like nickel and iron. The work presented here retains the key advantages demonstrated in our previous study on $FeNi_3$, including the use of a single, unchanged synthetic route for both OER and HER electrocatalysts, water as the reaction medium, low-temperature processing, and a rapid and straightforward work-up. Moreover, the electrochemical performance achieved is comparable to that of MEAs based on PGM electrocatalysts. In addition to these established benefits, the present approach offers enhanced environmental compatibility, arising from the use of aluminum powder as a benign and sustainable reducing agent. Although the results obtained in this study are promising, the present work should be regarded as a starting point for further optimization efforts. Future developments may focus on tailoring the $FeNi_3/FeNiO_x$ composition and structure to enhance HER activity, while carefully balancing performance improvements against process scalability and overall cost–benefit considerations. In parallel, optimization of the electrocatalyst loading on the electrodes represents an important parameter for further performance enhancement. AEMWE tests were conducted at the laboratory cell level; however, a more comprehensive investigation of catalyst degradation phenomena is necessary to properly assess long-term stability and support the potential scale-up from laboratory to pilot-scale and, subsequently, to industrial implementation.

5. Conclusions

In summary, a $FeNi_3/FeNiO_x$ nanosponge was successfully synthesized through a simple and scalable chemical reduction route employing aluminum powder as the reducing agent. Comprehensive structural and surface characterization was performed using XRD, SEM, XPS, HRTEM, and HAADF-STEM techniques. The electrocatalytic activity of $FeNi_3/FeNiO_x$ toward both HER and OER was systematically investigated by LSV, Tafel analysis, and single-cell AEMWE testing. The obtained performance was benchmarked against commercial PGM-based electrocatalysts, with particular attention to both mass-specific and geometric activity. The developed electrocatalyst delivers overpotentials of 97 mV for the HER and 254 mV for the OER at a current density of 10 mA cm^{-2} in 1 M KOH. The resulting PGM-free MEA, based on a single bifunctional electrocatalyst, outperforms a fully PGM-based configuration. In single-cell AEMWE tests, the MEA achieved a cell voltage of 2.037 V at 1 A cm^{-2} and 50 °C (without iR correction), corresponding to a voltage advantage of 105 mV over the PGM-based reference at the same current density. Furthermore, the system was operated for over 150 h under a daily power profile designed to emulate the intermittency of renewable energy sources. Overall, this work demonstrates an effective strategy for the development of high-performance, non-precious-metal-based MEAs relying on a single electrocatalyst, offering a promising pathway toward sustainable green hydrogen production.

CRediT authorship contribution statement

Francesko Malaj: Writing – original draft, Visualization, Validation, Resources, Methodology, Investigation, Funding acquisition, Formal analysis, Data curation, Conceptualization. **Domenico Lentini:** Methodology, Investigation, Formal analysis, Data curation, Conceptualization. **Alessandro Tampucci:** Supervision, Methodology, Investigation, Formal analysis, Conceptualization. **Lorenzo Brogi:** Resources, Methodology, Investigation, Formal analysis. **Raoul Cosenza:** Investigation, Formal analysis, Data curation. **Enrico Berretti:** Visualization, Methodology, Investigation, Data curation. **Mohsin Muhyuddin:** Writing – review & editing, Methodology, Formal analysis, Data curation. **Emmanuel De Gregorio:** Resources, Investigation, Data curation. **Gianluigi Baiardi:** Writing – review & editing, Methodology, Investigation, Formal analysis, Data curation. **Stiven Forti:** Writing – review & editing, Methodology, Investigation, Formal analysis, Data curation. **Antonio Rossi:** Resources, Methodology, Investigation, Formal analysis, Data curation. **Camilla Coletti:** Resources, Methodology, Investigation, Formal analysis, Data curation. **Maddalena Corsini:** Writing –

review & editing, Methodology, Investigation, Formal analysis, Data curation. **Oreste Tarallo:** Validation, Methodology, Investigation, Formal analysis, Data curation. **Francesco Ruffo:** Writing – review & editing, Supervision, Project administration, Investigation, Formal analysis, Data curation. **Carlo Santoro:** Writing – review & editing, Supervision, Project administration, Funding acquisition.

Declaration of competing interest

The authors declare that they have no known competing financial interests or personal relationships that could have appeared to influence the work reported in this paper.

Supplementary materials

Supplementary material associated with this article can be found, in the online version, at doi:10.1016/j.electacta.2026.148642.

References

[1] A.M. Oliveira, R.R. Beswick, Y. Yan, A green hydrogen economy for a renewable energy society, Curr. Opin. Chem. Eng. 33 (2021) 100701, https://doi.org/10.1016/j.coche.2021.100701.

[2] C. Santoro, A. Lavacchi, P. Mustarelli, V. Di Noto, L. Elbaz, D.R. Dekel, et al., What is Next in Anion-Exchange Membrane Water Electrolyzers? Bottlenecks, Benefits, and Future, ChemSusChem. 15 (8) (2022) e202200027, https://doi.org/10.1002/cssc.202200027.

[3] S. Shiva Kumar, V. Himabindu, Hydrogen production by PEM water electrolysis – A review, Mater. Sci. Energy Technol. 2 (3) (2019) 442–454, https://doi.org/10.1016/j.mset.2019.03.002.

[4] J. Brauns, T. Turek, Alkaline Water Electrolysis Powered by Renewable Energy: A Review, Processes 8 (2) (2020) 248, https://doi.org/10.3390/pr8020248.

[5] I. Vincent, D. Bessarabov, Low cost hydrogen production by anion exchange membrane electrolysis: A review, Int. J. Geogr. Inf. Sci. 81 (2018) 1690–1704, https://doi.org/10.1016/j.rser.2017.05.258.

[6] K.F.L. Hagesteijn, S. Jiang, B.P. Ladewig, A review of the synthesis and characterization of anion exchange membranes, J. Mater. Sci. 53 (16) (2018) 11131–11150, https://doi.org/10.1007/s10853-018-2409-y.

[7] W. You, K.J.T. Noonan, G.W. Coates, Alkaline-stable anion exchange membranes: A review of synthetic approaches, Prog. Polym. Sci. 100 (2020) 101177, https://doi.org/10.1016/j.progpolymsci.2019.101177.

[8] T. Caielli, A.R. Ferrari, S. Bonizzoni, E. Sediva, A. Caprì, M. Santoro, et al., Synthesis, characterization and water electrolyzer cell tests of poly(biphenyl piperidinium) Anion exchange membranes, J. Power. Sources. 557 (2023) 232532, https://doi.org/10.1016/j.jpowsour.2022.232532.

[9] M. Muhyuddin, C. Santoro, L. Osmieri, V.C.A. Ficca, A. Friedman, K. Yassin, et al., Anion-exchange-membrane electrolysis with alkali-free water feed, Chem. Rev. 125 (2025) 6906–6976, https://doi.org/10.1021/acs.chemrev.4c00466.

[10] A.H. Faqeeh, M.D. Symes, A standard electrolyzer test cell design for evaluating catalysts and cell components for anion exchange membrane water electrolysis, Electrochim. Acta 444 (2023) 142030, https://doi.org/10.1016/j.electacta.2023.142030.

[11] Y. Sugawara, S. Sankar, S. Miyanishi, R. Illathvalappil, P.K. Gangadharan, H. Kuroki, et al., Anion Exchange Membrane Water Electrolyzers: An Overview, J. Chem. Eng. Jpn. 56 (1) (2023) 2210195, https://doi.org/10.1080/00219592.2023.2210195.

[12] M. El-Shafie, Hydrogen production by water electrolysis technologies: A review, Results. Eng. 20 (2023) 101426, https://doi.org/10.1016/j.rineng.2023.101426.

[13] M.-I. Jamesh, X. Sun, Recent progress on earth abundant electrocatalysts for oxygen evolution reaction (OER) in alkaline medium to achieve efficient water splitting – A review, J. Power. Sources. 400 (2018) 31–68, https://doi.org/10.1016/j.jpowsour.2018.07.125.

[14] L. Trotochaud, S.L. Young, J.K. Ranney, S.W. Boettcher, Nickel–Iron Oxyhydroxide Oxygen-Evolution Electrocatalysts: The Role of Intentional and Incidental Iron Incorporation, J. Am. Chem. Soc. 136 (18) (2014) 6744–6753, https://doi.org/10.1021/ja502379c.

[15] M. Gong, H. Dai, A mini review of NiFe-based materials as highly active oxygen evolution reaction electrocatalysts, Nano Res. 8 (1) (2015) 23–39, https://doi.org/10.1007/s12274-014-0591-z.

[16] X. Yan, L. Tian, K. Li, S. Atkins, H. Zhao, J. Murowchick, et al., $FeNi_3$ /$NiFeO_x$ Nanohybrids as Highly Efficient Bifunctional Electrocatalysts for Overall Water Splitting, Adv. Mater. Interfaces. 3 (22) (2016) 1600368, https://doi.org/10.1002/admi.201600368.

[17] F. Malaj, A. Tampucci, D. Lentini, L. Brogi, E. Berretti, C. Coletti, et al., One-pot synthesis of FeNi3/FeNiOx nanoparticles for PGM-free anion exchange membrane water electrolysis, Electrochim. Acta 507 (2024) 145109, https://doi.org/10.1016/j.electacta.2024.145109.

[18] Q. Luo, M. Peng, X. Sun, Y. Luo, A.M. Asiri, Efficient electrochemical water splitting catalyzed by electrodeposited NiFe nanosheets film, Int. J. Hydrogen. Energy 41 (21) (2016) 8785–8792, https://doi.org/10.1016/j.ijhydene.2016.04.007.

[19] M. Guo, H. Meng, J. Jin, J. Mi, Amine-assisted synthesis of the Ni_3 Fe alloy encapsulated in nitrogen-doped carbon for high-performance water splitting, J. Mater. Chem. A 11 (12) (2023) 6452–6464, https://doi.org/10.1039/D2TA09549A.

[20] A.P. Reverberi, P.S. Varbanov, S. Lauciello, M. Salerno, B. Fabiano, An eco-friendly process for zerovalent bismuth nanoparticles synthesis, J. Clean. Prod. 198 (2018) 37–45, https://doi.org/10.1016/j.jclepro.2018.07.011.

[21] R. Jhajharia, D. Jain, A. Sengar, A. Goyal, P.R. Soni, Synthesis of copper powder by mechanically activated cementation, Powder. Technol. 301 (2016) 10–15, https://doi.org/10.1016/j.powtec.2016.05.031.

[22] G.D. Sulka, M. Jaskuła, Influence of the sulphuric acid concentration on the kinetics and mechanism of silver ion cementation on copper, Hydrometallurgy 77 (1–2) (2005) 131–137, https://doi.org/10.1016/j.hydromet.2004.10.016.

[23] S. Krishnan, N.S. Zulkapli, H. Kamyab, S.M. Taib, M.F.B.M. Din, Z.A. Majid, et al., Current technologies for recovery of metals from industrial wastes: An overview, Environ. Technol. Innov. 22 (2021) 101525, https://doi.org/10.1016/j.eti.2021.101525.

[24] J. Kim, R. Kim, K.N. Han, Advances in Hydrometallurgical Gold Recovery through Cementation, Adsorption, Ion Exchange and Solvent Extraction, Minerals 14 (6) (2024) 607, https://doi.org/10.3390/min14060607.

[25] A. Maimoni, Minerals recovery from salton sea geothermal brines: a literature review and proposed cementation process, Geothermics 11 (4) (1982) 239–258, https://doi.org/10.1016/0375-6505(82)90031-1.

[26] F. Malaj, D. Lentini, A. Tampucci, L. Brogi, E. Berretti, M. Muhyuddin, et al., A green approach to transition metal-based nanoparticles from aluminium powder cementation for application in OER electrocatalysis, Electrochim. Acta 536 (2025) 146805, https://doi.org/10.1016/j.electacta.2025.146805.

[27] D. Lentini, F. Malaj, A. Tampucci, L. Brogi, T. Caielli, P. Mustarelli, et al., Use of poly(styrene- co -acrylic acid) in a composite ion-solvating membrane for water electrolysis, ACS. Polym. Au 6 (2025) 256–266, https://doi.org/10.1021/acspolymersau.5c00126.

[28] W. Li, T. Cochell, A. Manthiram, Activation of Aluminum as an Effective Reducing Agent by Pitting Corrosion for Wet-chemical Synthesis, Sci. Rep. 3 (1) (2013) 1229, https://doi.org/10.1038/srep01229.

[29] E. McCafferty, Sequence of steps in the pitting of aluminum by chloride ions, Corros. Sci. 45 (7) (2003) 1421–1438, https://doi.org/10.1016/S0010-938X(02)00231-7.

[30] X. Lu, G. Liang, Y. Zhang, Synthesis and characterization of magnetic FeNi3 particles obtained by hydrazine reduction in aqueous solution, Mater. Sci. Eng.: B 139 (2–3) (2007) 124–127, https://doi.org/10.1016/j.mseb.2007.01.055.

[31] S. Anantharaj, S. Noda, Amorphous Catalysts and Electrochemical Water Splitting: An Untold Story of Harmony, Small. 16 (2) (2020) 1905779, https://doi.org/10.1002/smll.201905779.

[32] W. Cai, R. Chen, H. Yang, H.B. Tao, H.-Y. Wang, J. Gao, et al., Amorphous versus Crystalline in Water Oxidation Catalysis: A Case Study of NiFe Alloy, Nano Lett. 20 (6) (2020) 4278–4285, https://doi.org/10.1021/acs.nanolett.0c00840.

[33] Y. Yang, H. Fei, G. Ruan, C. Xiang, J.M. Tour, Efficient Electrocatalytic Oxygen Evolution on Amorphous Nickel–Cobalt Binary Oxide Nanoporous Layers, ACS. Nano 8 (9) (2014) 9518–9523, https://doi.org/10.1021/nn503760c.

[34] W.D. Chemelewski, H.-C. Lee, J.-F. Lin, A.J. Bard, C.B. Mullins, Amorphous FeOOH Oxygen Evolution Reaction Catalyst for Photoelectrochemical Water Splitting, J. Am. Chem. Soc. 136 (7) (2014) 2843–2850, https://doi.org/10.1021/ja411835a.

[35] J. Liu, M. Zhang, Q. Tang, Y. Zhao, J. Zhang, Y. Zhu, et al., Supra Hydrolytic Catalysis of Ni_3 Fe/rGO for Hydrogen Generation, Adv. Sci. 9 (21) (2022) 2201428, https://doi.org/10.1002/advs.202201428.

[36] M.C. Biesinger, L.W.M. Lau, A.R. Gerson, R.St.C Smart, The role of the Auger parameter in XPS studies of nickel metal, halides and oxides, Phys. Chem. Chem. Phys. 14 (7) (2012) 2434, https://doi.org/10.1039/c2cp22419d.

[37] A.N. Mansour, Characterization of NiO by XPS, Surf. Sci. Spectra 3 (3) (1994) 231–238, https://doi.org/10.1116/1.1247751.

[38] A.N. Mansour, Characterization of β -Ni(OH)2 by XPS, Surf. Sci. Spectra 3 (3) (1994) 239–246, https://doi.org/10.1116/1.1247752.

[39] A.N. Mansour, C.A. Melendres, Characterization of Electrochemically Prepared γ -NiOOH by XPS, Surf. Sci. Spectra 3 (3) (1994) 271–278, https://doi.org/10.1116/1.1247756.

[40] N.S. McIntyre, D.G. Zetaruk, X-ray photoelectron spectroscopic studies of iron oxides, Anal. Chem. 49 (11) (1977) 1521–1529, https://doi.org/10.1021/ac50019a016.

[41] S. Thoufeeq, P.K. Rastogi, S. Thomas, A. Shravani, T.N. Narayanan, M. R. Anantharaman, Single Step Grown NiFe Sponges as Efficient Water Splitting Electrocatalysts in Alkaline Medium, ChemistrySelect. 5 (4) (2020) 1385–1395, https://doi.org/10.1002/slct.202000112.

[42] J. Kibsgaard, I. Chorkendorff, Considerations for the scaling-up of water splitting catalysts, Nat. Energy 4 (6) (2019) 430–433, https://doi.org/10.1038/s41560-019-0407-1.

[43] F. Hu, S. Zhu, S. Chen, Y. Li, L. Ma, T. Wu, et al., Amorphous Metallic NiFeP: A Conductive Bulk Material Achieving High Activity for Oxygen Evolution Reaction in Both Alkaline and Acidic Media, Adv. Mater. 29 (32) (2017) 1606570, https://doi.org/10.1002/adma.201606570.

[44] E. Hatami, A. Toghraei, G. Barati Darband, Electrodeposition of Ni–Fe micro/nano urchin-like structure as an efficient electrocatalyst for overall water splitting, Int. J. Hydrogen. Energy 46 (14) (2021) 9394–9405, https://doi.org/10.1016/j.ijhydene.2020.12.110.

[45] R. Xin, Y. Liu, X. Li, S. Yi, M. Zhang, H. Chen, et al., Low-temperature pyrolysis enables $FeNi_3$ nanoparticle implanted N-doped carbon nanosheets as an efficient bifunctional electrocatalyst for overall water splitting, J. Mater. Chem. A 11 (26) (2023) 14015–14024, https://doi.org/10.1039/D3TA01819A.
[46] M. Ďurovič, J. Hnát, K. Bouzek, Electrocatalysts for the hydrogen evolution reaction in alkaline and neutral media. A comparative review, J. Power. Sources. 493 (2021) 229708, https://doi.org/10.1016/j.jpowsour.2021.229708.
[47] Y. Ni, W. Zhang, Y. Li, S. Hu, H. Yan, S. Xu, Ultralow-content Pt nanodots/Ni_3 Fe nanoparticles: interlayer nanoconfinement synthesis and overall water splitting, Nanoscale 16 (15) (2024) 7626–7633, https://doi.org/10.1039/D4NR00029C.
[48] Y. Hu, T. Xiong, M.-S.J.T. Balogun, Y. Huang, D. Adekoya, S. Zhang, et al., Enhanced metallicity boosts hydrogen evolution capability of dual-bimetallic Ni–Fe nitride nanoparticles, Mater. Today Phys. 15 (2020) 100267, https://doi.org/10.1016/j.mtphys.2020.100267.
[49] K.S. Exner, On the mechanistic complexity of oxygen evolution: potential-dependent switching of the mechanism at the volcano apex, Mater. Horiz. 10 (6) (2023) 2086–2095, https://doi.org/10.1039/D3MH00047H.
[50] E. Taibi, H. Blanco, R. Miranda, M. Carmo, Green Hydrogen Cost Reduction: Scaling up Electrolysers to Meet the 1.5° C Climate Goal, Abu Dhabi, Irena, 2020.
[51] P. Nuss, M.J. Eckelman, Life Cycle Assessment of Metals: A Scientific Synthesis, PLoS. One 9 (7) (2014) e101298, https://doi.org/10.1371/journal.pone.0101298.